

# 1 Variability and trend analysis of temperature and height in the upper 2 troposphere and stratosphere region over the tropics (Réunion), by 3 combining balloon-sonde and satellite measurements

4 Gregori de Arruda Moreira<sup>1</sup>, Hassan Bencherif<sup>2</sup>, Tristan Millet<sup>2</sup>, Damaris Kirsch Pinheiro<sup>3</sup>

5 <sup>1</sup>Federal Institute of Education, Science and Technology of São Paulo (IFSP), São Paulo, 01109-010, Brazil

6 <sup>2</sup>Laboratoire de l'Atmosphère et des Cyclones (LACy, UMR 8105 CNRS, Université de La Réunion, Météo-France), Reunion  
7 Island, France

8 <sup>3</sup>Federal University of Santa Maria, Santa Maria, 97105-900, Brazil

9 *Correspondence to:* Gregori de Arruda Moreira (gregori.moreira@ifsp.edu.br)

10 **Abstract.** Tropopause height and temperature play a crucial role in atmospheric chemistry and radiative forcing and serve as  
11 key indicators of anthropogenic climate change. However, accurately determining this parameter requires advanced remote  
12 sensing techniques. This study compares tropopause height and temperature estimated from in-situ and remote sensing  
13 instruments (SHADOZ and COSMIC-1) with reanalysis data from MERRA-2 over Réunion from 2006 to 2020. The results  
14 reveal strong agreement between vertical temperature profiles obtained from SHADOZ and COSMIC-1, demonstrating that  
15 both can reliably estimate tropopause height using the Cold Point Temperature (CPT) and/or Lapse Rate Temperature (LRT)  
16 methods. Conversely, while MERRA-2 assimilates data from these sources, its fixed vertical resolution limits its ability to  
17 capture tropopause height variations accurately. Given the consistency between SHADOZ and COSMIC-1, their data were  
18 combined to construct a more refined dataset, which was then used to assess temperature trends. The analysis indicates a high  
19 influence of annual and semi-annual oscillations in Tropopause height dynamics, as well as, a decreasing trend in CPT and a  
20 slight increase in the Lapse Rate Tropopause (LRT) height.

## 21 1 Introduction

22 The troposphere is the atmospheric layer extending from the Earth's surface to around 18 km, depending on the latitude, so it  
23 is generally higher at the equator and decreases toward the poles. Inside this layer can be found the Tropical Tropopause Layer  
24 (TTL), which extends from 12-14 to 18 km, and it represents the transition region between the well-mixed convective  
25 troposphere and the radiatively controlled stratosphere (Fueglistaler et al., 2009; Randel and Jensen, 2013). The TTL is the

26 main gateway for air to enter the stratosphere and a crucial indicator of anthropogenic climate change, as indicated by variations  
27 in the height and/or temperature of the tropopause (Astudillo et al., 2014; Santer et al., 2004).

28 The tropopause, found within the TTL, is a significant physical boundary that separates the unstable and moist troposphere  
29 from the stable and dry stratosphere. The temperature and height of such layer are influenced by both tropospheric and  
30 stratospheric forcing, like as changes in solar radiation (Reid and Gage, 1981), atmospheric angular momentum (Reid and  
31 Gage, 1984), El Niño-Southern Oscillation (ENSO), stratospheric ozone (Hoinka, 1998), Quasi-Biennial Oscillation (QBO)  
32 variability, explosive volcanic eruptions (Reid and Gage, 1985; Randel et al., 2000), and concentrations of Greenhouse Gases  
33 (GHG) (Zou et al., 2023). Consequently, tropospheric warming or stratospheric cooling can result in an increase in the  
34 tropopause height (Astudillo et al., 2014; Santer et al., 2004).

35 Traditional methods for sounding tropopause structure are usually based on in situ measurements (e.g., weather stations,  
36 radiosonde), model data (e.g., reanalysis data) and remote sensing (e.g., lidar, airborne, satellite soundings). The direct  
37 sounding technique usually has an uneven global distribution, with only sparse data distribution, especially in the southern  
38 hemisphere (Santer et al., 2004). On the other hand, reanalyses provide global and temporal coverage and a uniform data type  
39 (Xian and Homeyer, 2019). However, reanalyses suffer from coarser vertical resolution, which can render tropopause height  
40 detection unfeasible (Birner et al. 2006). Considering remote sensing, Global Navigational Satellite System Radio Occultation  
41 (GNSS-RO) stands out for offering accurate tropospheric profiles with high vertical resolution and global coverage  
42 independently of weather conditions. However, they are endowed with lower temporal resolution. Therefore, considering the  
43 limitations and advantages of each methodology, an option to improve the tropopause monitoring is to combine them. Although  
44 firstly it is necessary to identify their similarities and differences.

45 In this context, this study compares vertical temperature profiles from the Southern Additional Ozonesondes (SHADOZ)  
46 network, Constellation Observing System for Meteorology Ionosphere and Climate 1 (COSMIC-1), and Modern Era  
47 Retrospective analysis for Research and Applications – Version 2 (MERRA-2) over Réunion (2006–2020) to identify  
48 similarities and/or differences. Additionally, the study demonstrates how these datasets contribute to understanding variability  
49 in the Upper Troposphere–Lower Stratosphere (UT-LS) region. Finally, by combining ground-based balloon-sonde data and  
50 satellite-based COSMIC-1 observations, the variability and trend estimate of temperature in the tropical UT-LS region were  
51 investigated.

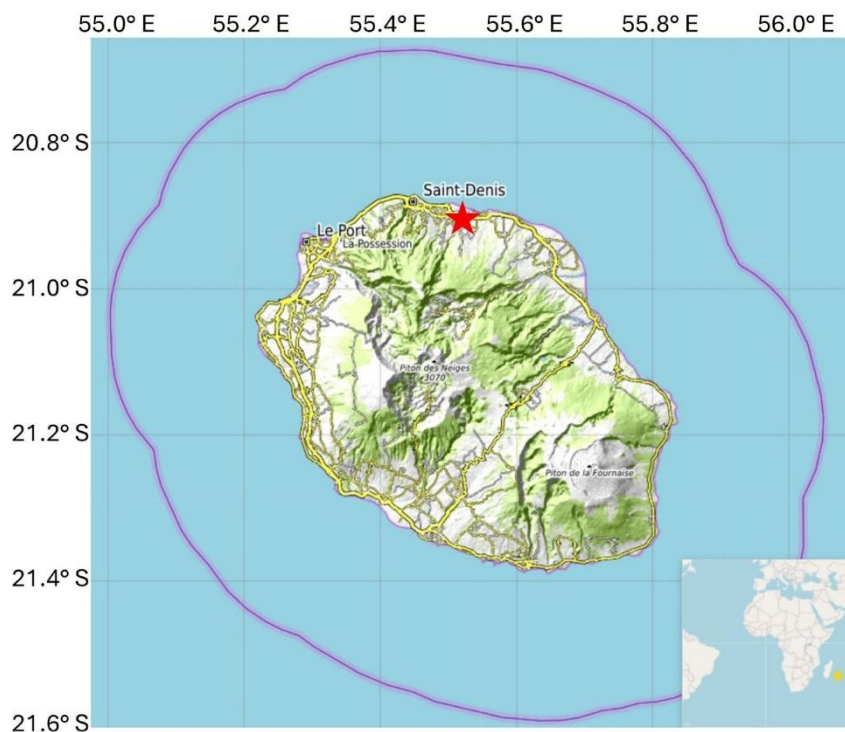
52 The paper structure is as follows: Section 2 gives a brief description of the experimental site and instruments used. The  
53 methodologies applied are presented in section 3. The comparisons between temperatures and tropopause height estimated

54 from SHADOZ, COSMIC-1 and MERRA-2 datasets are presented in section 4. In section 5, the results provided by the Trend-  
55 Run model are described. Finally, the conclusions are given in Section 6.

## 56 2 Materials

### 57 2.1 Study Area

58 Réunion (Fig. 1) is a volcanic island of the Indian Ocean with a population of ~860,000 inhabitants. It covers around 2,512  
59 km<sup>2</sup>, and it is characterized by a humid tropical climate tempered by the oceanic influence of the trade winds blowing from the  
60 southeast. In addition, this climate is endowed with great variability, mainly due to the island landscape, which causes  
61 numerous microclimates (Britannica, 2025).



62  
63 **Figure 1: Geographical location of the study site, Réunion, a French overseas department in the southern tropics. The red star**  
64 **symbol indicates the measurement site where the balloon radiosondes are carried out, located to the north of the island at Roland**  
65 **Garros International Airport (20.9° S; 55.5° E).**

### 66 2.2 Measurement by ballon-sonde experiment

67 Radiosonde measurements began in Réunion in 1993 (Baldy et al., 1996), and the station joined the Southern Hemisphere  
68 ADDitional OZonesondes (SHADOZ) network in 1998, increasing the frequency of measurements to weekly. The SHADOZ  
69 network is a NASA project that aims to fill gaps in ozone observation in the southern tropics by increasing radiosonde

70 frequencies at existing stations on a cost-sharing basis (Thompson et al., 2003). Each radiosonde is coupled in a balloon  
71 meteorological sonde, with an electrochemical cell (ECC) ozone-sonde, to transmit in-situ information on air pressure,  
72 temperature, relative humidity, and ozone partial pressure (Witte et al., 2017). The radiosonde technique has as its main  
73 disadvantages the limited spatial and temporal resolution, which can hinder a detailed observation of the dynamics of the  
74 tropopause. For this study, we used radiosonde temperature profiles from the study site (2006–2020), covering the COSMIC-  
75 1 mission's operational period and overlapping with its measurements. Radiosonde data can be accessed at the following link  
76 on the SHADOZ website (<https://tropo.gsfc.nasa.gov/shadoz/Reunion.html>).

### 77 **2.3 Temperature profiles from the COSMIC-1 experiment**

78 The Constellation Observing System for Meteorology, Ionosphere, and Climate 1 (COSMIC-1) is a joint U.S.-Taiwanese  
79 program designed to provide advances in meteorology, ionospheric research, climatology, and space weather by using GNSS-  
80 RO, which is a satellite remote sensing technique that uses GNSS (e.g. Global Positioning System - GPS) measurements  
81 received by low-Earth orbiting satellites to profile the Earth's atmosphere and ionosphere with high vertical resolution and  
82 global coverage (Thompson et al., 2003; Anthes et al., 2008). The COSMIC-1 was launched into a circular low-Earth orbit on  
83 April 15, 2006, and retired in 2020. Its main limitation is the data gap during maintenance periods and after the beginning of  
84 the progressive degradation, which began in 2019 and resulted in total inoperability in May 2020. In this paper, we utilized all  
85 temperature profiles that have been provided by COSMIC-1 between 2006 and 2020. The profiles were selected for a specific  
86 geographic area, covering Réunion with a margin of  $\pm 2^\circ$  in latitude and  $\pm 3^\circ$  in longitude.

### 87 **2.4 Temperature assimilation from the MERRA-2 reanalysis**

88 The Modern-Era Retrospective Analysis for Research and Applications – Version 2 (MERRA-2) is a global atmospheric  
89 reanalysis produced by the National Aeronautics and Space Administration (NASA) Global Modeling and Assimilation Office  
90 (GMAO). MERRA-2 replaces the original MERRA so that more information is assimilated, such as modern hyperspectral  
91 radiance and microwave observations, along with GPS-Radio Occultation and NASA ozone datasets. Like COSMIC-1 time  
92 cover, we used vertical temperature profiles from MERRA-2 data from 2006 to 2020. Such temperature profiles can be  
93 obtained from the following MERRA-2 product, M2T3NVASM\_5.12.4  
94 ([https://disc.gsfc.nasa.gov/datasets/M2T3NVASM\\_5.12.4/summary](https://disc.gsfc.nasa.gov/datasets/M2T3NVASM_5.12.4/summary)), which is composed of 17 atmospheric variables and has  
95 a spatial resolution of  $0.5^\circ \times 0.625^\circ$ . All data are distributed on 72 pressure levels, ranging from 1000 to 0.01 hPa, with a time  
96 resolution of 3 hours. These fixed heights can make it impossible to adequately observe some variations and trends in the  
97 tropopause behaviour (Zou et al., 2023). In this study, we used MERRA-2 average daily temperature profiles.

### 98 **3 Methods**

99 This study is based on the combination of 3 sources of temperature profile data at Réunion (radiosonde, COSMIC-1 and  
100 MERRA-2), over 15 years (2006-2020). Such a combination makes it possible to describe the thermal structure of the tropical  
101 atmosphere from the ground up to the mesosphere. However, given the differences in the methods of acquisition and  
102 production, the temperature data used may not offer the same uncertainties, or resolutions everywhere at all altitudes and in  
103 all seasons. The first step is to compare these datasets to each other and define the altitude ranges where they can be used with  
104 confidence. Secondly, one could use all or a combination of these data to construct a coherent and regular time series, to  
105 investigate variability and temperature change in different atmospheric layers. Regarding the values obtained from the methods  
106 described in the following subsections, all reported uncertainties represent  $\pm 2\sigma$  variability unless stated otherwise.

#### 107 **3.1 Cold-Point Tropopause**

108 Based on thermal properties, it is possible to use the temperature profile to estimate the tropopause height from the Cold-Point  
109 Tropopause ( $TH_{CPT}$ ), which can be defined as the height where the tropospheric temperature reaches its minimum value  
110 (Selkrik, 1993). In this paper, the temperature observed at this height  $z$  is denominated  $T_{CPT}$ . Such definition is given by the  
111 following equation:

$$112 \quad T(z) \begin{cases} T_{CPT} = \min(T(z)) \\ TH_{CPT} = z, \\ \text{where } T(z) = T_{CPT} \end{cases} \quad (1)$$

#### 113 **3.2 Lapse-Rate Tropopause**

114 From temperature profiles  $T(z)$  it is possible to identify the tropopause height from the lowest level at which the lapse rate is  
115 less than  $2 \text{ K.km}^{-1}$  and it remains within this level for the next 2 km, such a point is denominated as the Lapse-Rate Tropopause  
116 ( $TH_{LRT}$ ) (WMO,1957), which is endowed of high stability, and signifies the thermodynamical transition between the  
117 troposphere and stratosphere. In this paper, the temperature detected at such height is denominated  $T_{LRT}$ . In addition, in all

118 cases of the final time series where the criterium established in the previous paragraph was not identified, the  $TH_{LRT}$  was  
119 classified as NaN.

### 120 3.3 Stratopause Height

121 As defined by France et al. (2012), the stratopause is determined as the altitude where the stratospheric temperature reaches  
122 its maximum in the vicinity of 50 km. Therefore, considering the 3 databases applied in this study, only the COSMIC-1  
123 temperature profiles can be used to detect the stratopause, due to their vertical range and resolution.

### 124 3.4 Forcings parametrization in the Trend-Run model

125 The Trend-Run model, a multiple linear regression model, was first adapted at the University of Réunion to analyse  
126 temperature trends in the southern subtropical upper troposphere-lower stratosphere (UT-LS) (Bencherif et al., 2006). This  
127 model decomposes the variations of a time-series signal,  $S(t)$ , into components representing atmospheric forcings:

$$128 \quad 129 \quad S(t) = c_1SAO(t) + c_2AO(t) + c_3QBO(t) + c_4ENSO(t) + c_5SSN(t) + c_6IOD(t) + \varepsilon \quad (2)$$

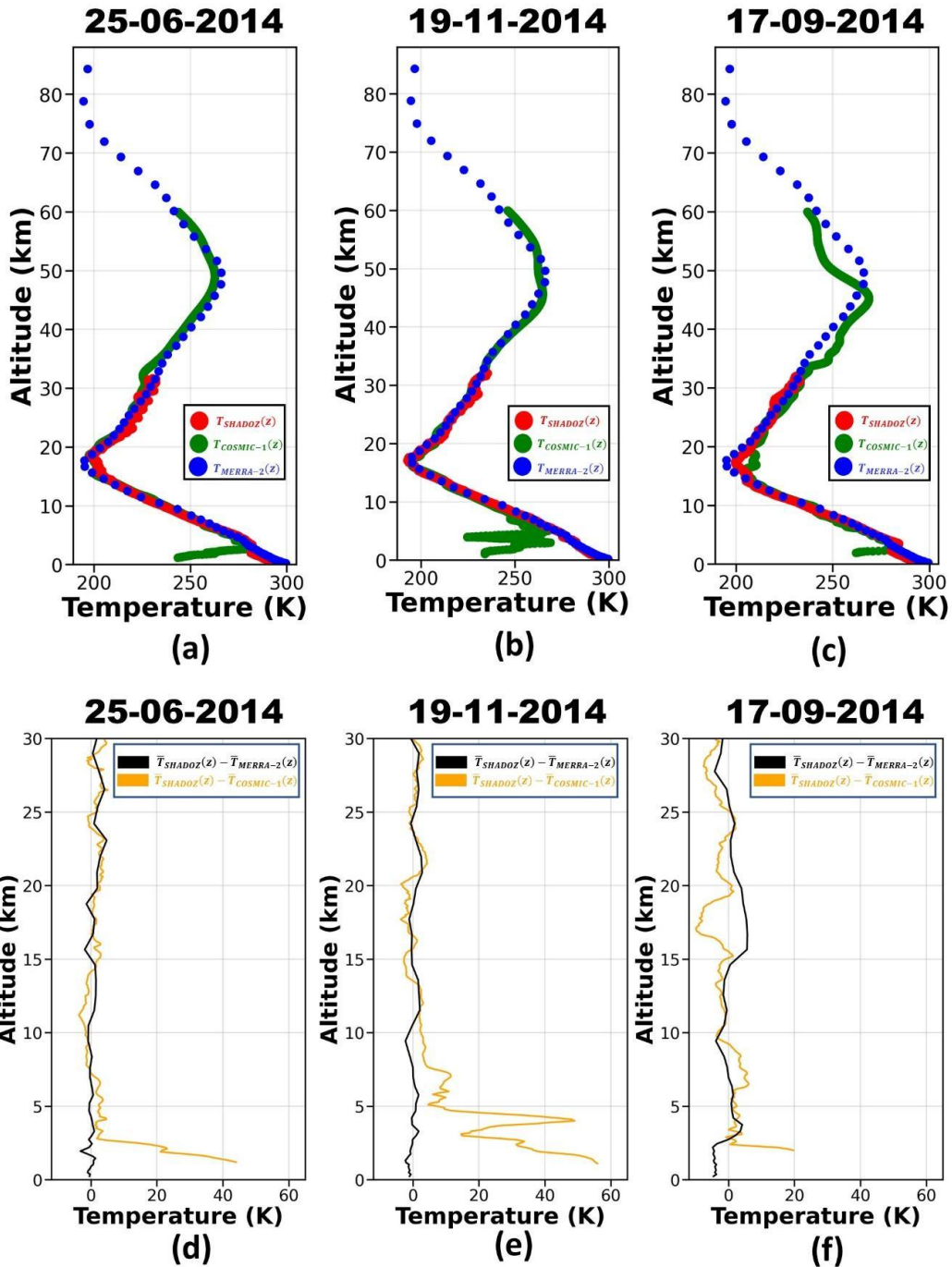
130  
131 where  $\varepsilon$  represents the residuals term which includes the trend, and  $c_i$  (i ranging from 1 to 6) are contribution coefficients of  
132 the respective forcings. The coefficients  $c_i$  can be derived using the least-squares method, which minimizes the residual  
133 variance, while the trend is parameterized as linear:  $Trend(t) = a_0 + a_1t$ , where  $a_0$  is a constant, and  $a_1$  is the trend slope.  
134 The initial model incorporated key forcings, including annual and semi-annual oscillations (AO, SAO), quasi-biennial  
135 oscillation (QBO), El Niño-Southern Oscillation (ENSO), sunspot numbers (SSN), AO and SAO represent seasonal cycles,  
136 with SAO being particularly dominant in the tropics above 35 km altitude. SAO amplitudes decrease with latitude but can  
137 intensify in the subtropics, depending on altitude. QBO is parametrised as a proxy of the zonal wind at 70 hPa derived from  
138 balloon measurements at the Equator (Singapore), while the ENSO is parametrized with the Multivariate ENSO Index (Randel  
139 and Cobb, 1994). The model was further extended by Bègue et al. (2010) to include the Indian Ocean Dipole (IOD), which  
140 describes sea surface temperature (SST) anomalies in the Indian Ocean's east-west dipole (Saji et al., 1999; Morioka et al.,  
141 2010). The IOD, measured by the Dipole Mode Index (DMI), quantifies the SST difference between the western (50°E–70°E,  
142 10°S–10°N) and eastern (90°E–110°E, 10°S–Equator) Indian Ocean (Sivakumar et al., 2017). The DMI data were sourced  
143 from the Japanese Agency for Marine-Earth Science and Technology. The model's performance, measured with the coefficient  
144 of determination ( $R^2$ ), evaluates its ability to explain how much the forcings explain the signal variability. Decadal temperature  
145 trends (in Kelvin) were calculated to evaluate long-term changes. For details on the Trend-Run model and its parameterizations,  
146 see Bencherif et al. (2006) and Bègue et al. (2010).

147 **4 Analysis of temperature profiles**

148 In this section, a comparison is performed among the vertical temperature profiles provided by MERRA-2 ( $T_{MERRA-2}(z)$ ),  
149 SHADOZ ( $T_{SHADOZ}(z)$ ) and COSMIC-1 ( $T_{COSMIC-1}(z)$ ). The limitations and advantages of each system will be presented and  
150 then a database will be created combining the data from the instruments that are endowed of the most similar profiles.

151 **4.1 Day-to-day Comparisons**

152 Figure 2 shows daily comparisons of vertical temperature profiles from SHADOZ ( $T_{SHADOZ}(z)$ ), COSMIC-1 ( $T_{COSMIC-1}(z)$ ),  
153 and MERRA-2 ( $T_{MERRA-2}(z)$ ) for three selected dates: 25 June 2014 (Fig. 2a), 19 November 2014 (Fig. 2b), and 17 September  
154 2014 (Fig. 2c). The corresponding temperature differences (SHADOZ – COSMIC-1 and SHADOZ – MERRA-2) for the same  
155 dates are presented in Figures 2d, 2e, and 2f.



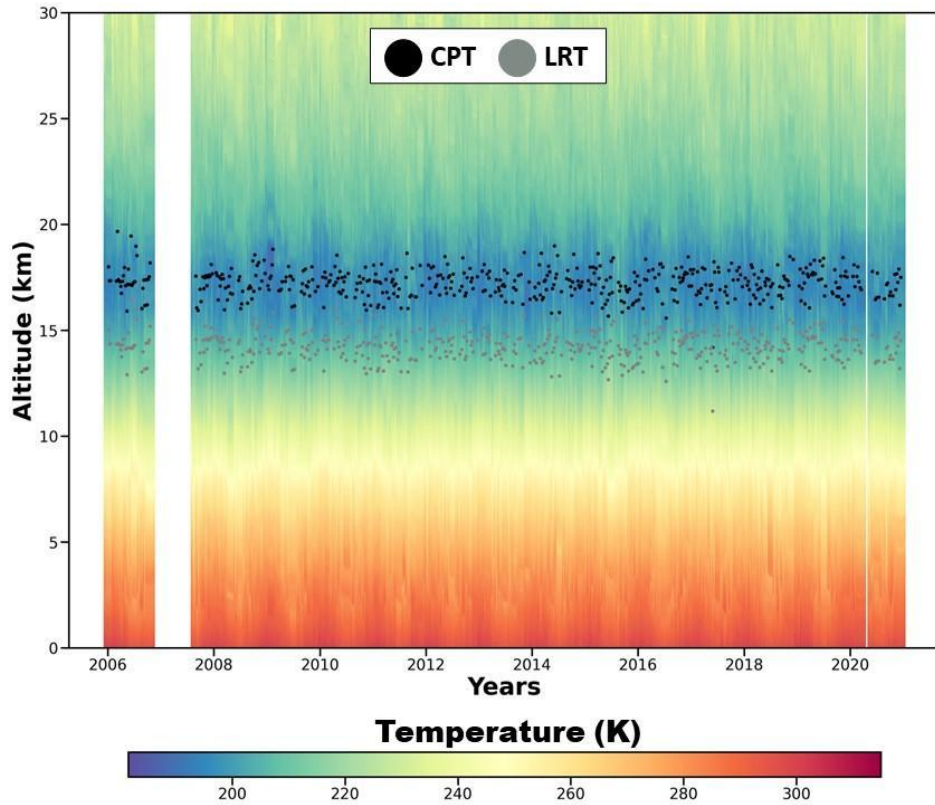
156

157 Figure 2: Comparison between  $T_{SHADOZ}(z)$  (red),  $T_{COSMIC-1}(z)$  (green) and  $T_{MERRA-2}(z)$  (blue) profiles on 25-06-2014 (a), 19-11-  
 158 2014 (b) and 17-09-2014 (c) and the difference between  $T_{SHADOZ}(z)$  and  $T_{COSMIC-1}(z)$  (orange line) and  $T_{SHADOZ}(z)$  and  
 159  $T_{MERRA-2}(z)$  (black line) profiles to the same days (d), (e), and (f), respectively.

160 On 25 June and 19 November, the difference between  $T_{SHADOZ}(z)$  and  $T_{MERRA-2}(z)$  does not exceed 4.0 K, so that the minimal  
161 differences are observed below 6.0 km and in the region between 16.0 km and 18.0 km. On the other hand,  $T_{SHADOZ}(z)$  and  
162  $T_{COSMIC-1}(z)$  present a significant difference below 5.0 km (in some points the difference is higher than 40.0 K). However,  
163 above 10.0 km, on both days,  $T_{SHADOZ}(z)$  and  $T_{COSMIC-1}(z)$  are very similar, so that the difference does not exceed 5.0 K.  
164 On 17 September,  $T_{SHADOZ}(z)$  and  $T_{MERRA-2}(z)$  present a difference lower than 5.0 K in the region below 15.0 km. Above  
165 15.0 km, the difference increases significantly, mainly in the region between 15.0 and 20.0 km. As observed in the other two  
166 days, the higher difference between  $T_{SHADOZ}(z)$  and  $T_{COSMIC-1}(z)$  is observed in the first 5.0 km. However, a significant  
167 difference (around 6 K) also is observed in the region between 15.0 and 20.0 km, resulting in a variation of approximately 2.1  
168 km between the CPT estimated by  $T_{SHADOZ}(z)$  (17.3 km) and  $T_{COSMIC-1}(z)$  (15.2 km). In addition, a difference between  
169  $T_{COSMIC-1}(z)$  and  $T_{MERRA-2}(z)$  in the region above 30.0 km is significantly higher than that observed in previous analyses.  
170 However, as will be demonstrated in the next sections, it is possible to consider 17 September as an exceptional case, where  
171  $T_{COSMIC-1}(z)$  presents an abnormal behavior.

#### 172 **4.2 Weekly (SHADOZ) and daily (COSMIC-1) temperature profiles**

173 Figure 3 presents the curtain plot from the ground up to 30.0 km of weekly temperature profiles as measured by balloon-sondes  
174 ( $T_{SHADOZ}$ ) at Réunion from 2006 to 2020. The figure shows that during this period, balloon-sonde measurements at Réunion  
175 were carried out almost continuously, at the rate of one release per week, except in 2007, due to a shortage of stock supplies,  
176 which resulted in a 3-month interruption. For each profile, the tropopause height was determined and corresponds to the  
177 location of the LRT ( $LRT_{SHADOZ}$ ) and CPT ( $CPT_{SHADOZ}$ ), as defined above. Their respective positions are superimposed in  
178 Figure 3 by grey and black dots. Overall, the altitude of the  $CPT_{SHADOZ}$  varies between 16.0 and 19.0 km, with an average  
179 position of  $[17.2 \pm 1.4]$  km, while the  $LRT_{SHADOZ}$  varies between 14.0 and 16.0 km, with an average value of  $[14.9 \pm 1.5]$  km,  
180 resulting in an average difference of  $[2.3 \pm 0.3]$  between  $CPT_{SHADOZ}$  and  $LRT_{SHADOZ}$ . The range of  $CPT_{SHADOZ}$  values agrees  
181 with the results reported by Bègue et al. (2010), and with the average value obtained by Sivakumar et al. (2006)  $[17.2 \pm (1\sigma)$   
182  $0.6]$  km. On the other hand, the  $LRT_{SHADOZ}$  range is below of Bègue et al. (2010) results, as well as the average value is lower  
183 than that one reported by Sivakumar et al. (2006)  $[16.0 \pm (1\sigma) 0.7]$  km. Consequently, the average difference between  
184  $CPT_{SHADOZ}$  and  $LRT_{SHADOZ}$  is higher than the values obtained by Bègue et al. (2010), Sivakumar et al. (2006), and Zhran et al.  
185 (2023)  $[0.91 \pm (1\sigma) 0.15]$  km,  $[1.09 \pm (1\sigma) 0.94]$  km, and 0.92 km, respectively. It is important to highlight that the number of  
186  $LRT_{SHADOZ}$  cases are lower than those of  $CPT_{SHADOZ}$ , as not all  $T_{SHADOZ}(z)$  profiles have the essential characteristics for  
187 calculating the LRT.



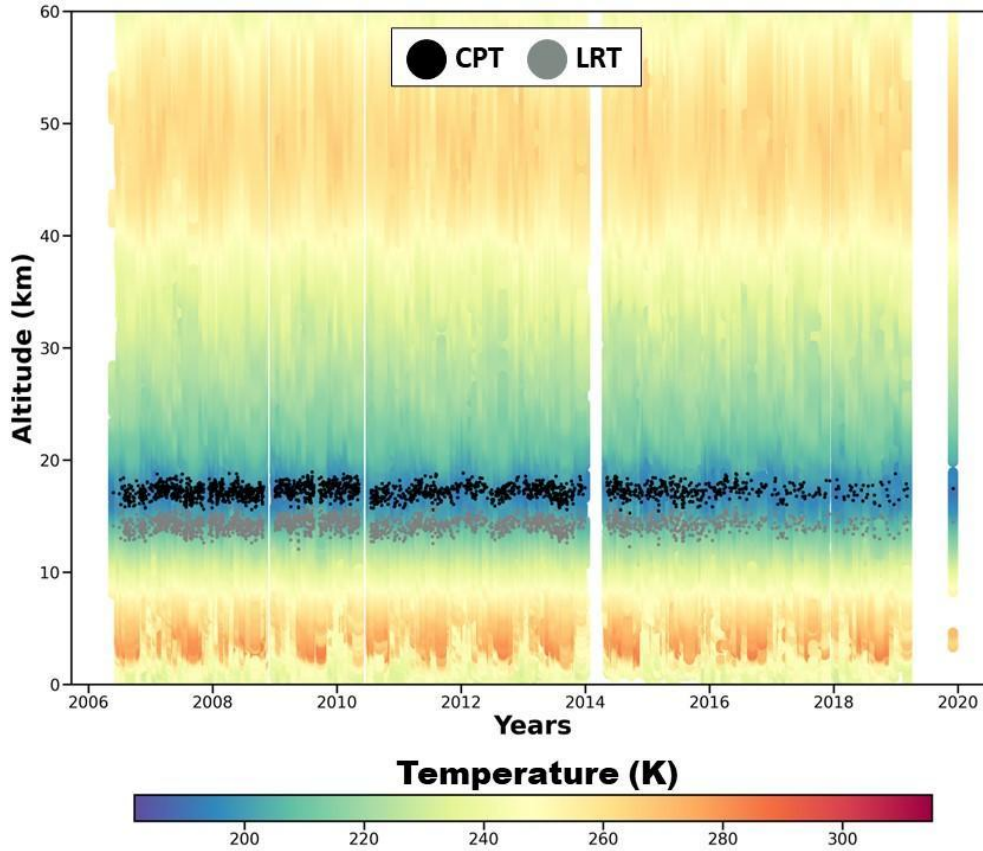
188

189 **Figure 3: Time-height temperature cross-section over Réunion from weekly balloon-sonde profiles from January 2006 to December**  
 190 **2020. Black and gray dots indicate the CPT and LRT heights, respectively.**

191 Similar to Figure 3, Figure 4 presents the curtain plot of the vertical temperature profiles from the surface to 60.0 km height,  
 192 as derived from daily COSMIC-1 measurements from 2006 to 2020. By comparison to SHADOZ temperature profiles,  
 193 COSMIC-1 profiles present a higher vertical range, up to the mesosphere (limited here to 60.0 km) with greater temporal  
 194 sampling. Table 1 presents the total number of temperature profiles per month used in the present study from SHADOZ and  
 195 COSMIC-1 measurements. COSMIC-1 presents a lack of data in February and March 2014, and from June to December 2019.  
 196 In addition, based on the density of CPT and LRT points in Figure 4, it can be noted that there was a decrease in the number  
 197 of COSMIC-1 overpasses over the study site from 2017.

198 A quick visual comparison of the  $T_{SHADOZ}$  (Figure 3) and the  $T_{COSMIC-1}$  (Figure 4) shows significant differences below 10 km  
 199 altitude. The CPT values obtained from COSMIC-1 data ( $CPT_{COSMIC-1}$ ) are located in the same range of  $CPT_{SHADOZ}$ , so that  
 200 the average value provided by COSMIC-1 data [ $17.2 \pm 1.3$ ] km is similar to average  $CPT_{SHADOZ}$  [ $17.2 \pm 1.4$ ] km and almost  
 201 identical to the value obtained by Sivakumar et al. (2006). Regarding the LRT ( $LRT_{COSMIC-1}$ , the range of values [between  
 202 14.0 and 16.0 km] and the average value [ $14.7 \pm 1.2$ ] km) are similar to that one obtained from SHADOZ data, consequently  
 203 the average difference between  $CPT_{COSMIC-1}$  and  $LRT_{COSMIC-1}$  [ $2.9 \pm 1.9$ ] km is similar to that one observed between the

204 SHADOZ data. These results agree with those presented by Xia et al (2021), who found an average difference of 2.67 km  
 205 between  $CPT_{COSMIC-1}$  and  $LRT_{COSMIC-1}$ .

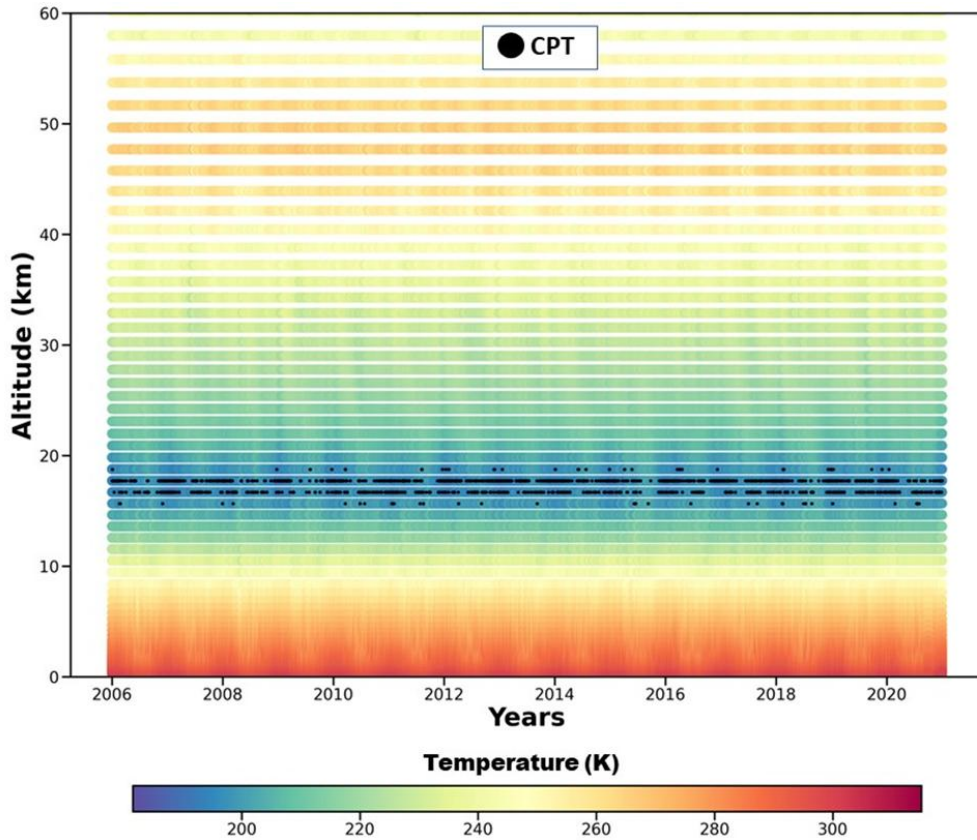


206  
 207 **Figure 4: Same as Figure 3 but concerning COSMIC-1 measurements over Réunion.**

208  
 209 **Table 1: Total monthly number of temperature profiles used from SHADOZ and COSMIC-1 measurements at the Réunion site.**

|                 | <i>JAN</i> | <i>FEB</i> | <i>MAR</i> | <i>APR</i> | <i>MAY</i> | <i>JUN</i> | <i>JUL</i> | <i>AUG</i> | <i>SEP</i> | <i>OCT</i> | <i>NOV</i> | <i>DEC</i> | <i>Total</i> |
|-----------------|------------|------------|------------|------------|------------|------------|------------|------------|------------|------------|------------|------------|--------------|
| <i>SHADOZ</i>   | 40         | 43         | 46         | 46         | 45         | 53         | 30         | 24         | 54         | 48         | 43         | 32         | 504          |
| <i>COSMIC-1</i> | 159        | 163        | 197        | 175        | 158        | 169        | 223        | 216        | 162        | 164        | 112        | 99         | 1997         |

210  
 211 In contrast to SHADOZ and COSMIC-1 data, MERRA-2 does not show any data gap (Fig. 5). Although the  $T_{MERRA-2}$  have a  
 212 reasonable agreement with  $T_{SHADOZ}$  and  $T_{COSMIC-1}$  in tropopause region (Fig. 2), MERRA-2 data cannot be used to detect the  
 213 tropopause height accurately, because the heights are fixed, as mentioned previously, then the results obtained have low  
 214 variability, making it impossible to observe the variations and trends in this layer (Fig. 5). Zou et al. (2023), when comparing  
 215 CPT and LRT values using different reanalysis databases (ERA-Interim, MERRA-2 and NCEP/NCAR Reanalysis 1), also  
 216 address the difficulty of refinement due to the coarser vertical resolution.



217

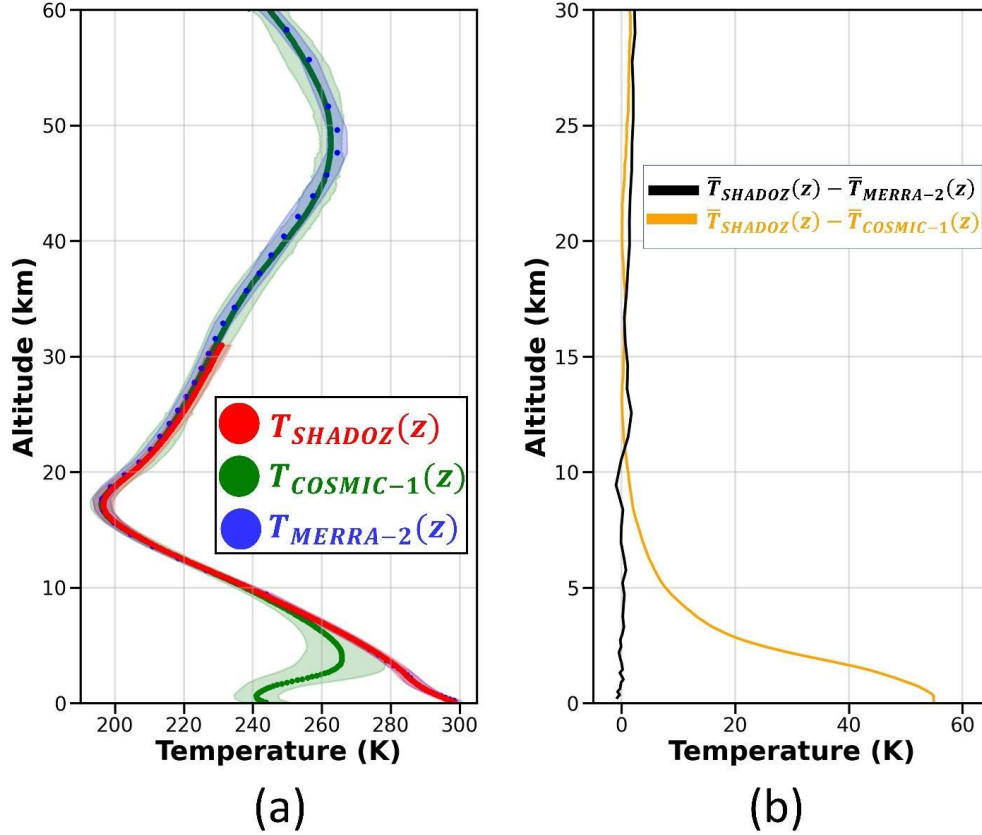
218 **Figure 5: Time-height temperature cross-section over Réunion from daily MERRA-2 data from January 2006 to December 2020.**  
 219 **The black dots indicate the CPT.**

### 220 4.3 Global Comparison

221 In this subsection, the global mean temperature profiles obtained from the 3 datasets (SHADOZ, COSMIC-1 and MERRA-2)  
 222 were computed and compared with each other. A global temperature profile is obtained by averaging all the temperature  
 223 profiles recorded by the same experiment over the entire study period (2006-2020). We thus obtained 3 global average profiles  
 224 for the 3 datasets:  $\bar{T}_{SHADOZ}(z)$ ,  $\bar{T}_{COSMIC-1}(z)$ , and  $\bar{T}_{MERRA-2}(z)$ . They are superimposed in Figure 6(a), respectively in red,  
 225 green and blue dots. Figure 6(b) shows the temperature differences in the 0.0 - 30.0 km altitude range between the COSMIC-1  
 226 and MERRA-2 global profiles and the SHADOZ global profile:  $(\bar{T}_{SHADOZ}(z) - \bar{T}_{COSMIC-1}(z))$  and  $(\bar{T}_{SHADOZ}(z) -$   
 227  $\bar{T}_{MERRA-2}(z))$ , respectively in orange and black lines. Using SHADOZ data as a reference, it is evident that COSMIC-1  
 228 temperature values progressively overestimate as height decreases below 8.0 km, whereas MERRA-2 assimilated temperatures  
 229 show excellent agreement. The largest differences are obtained between SHADOZ and COSMIC-1 values in the lower  
 230 troposphere, up to 55.0 K near the surface (see Figure 6b).

231 Above 10.0 km, the differences between  $\bar{T}_{COSMIC-1}$  and  $\bar{T}_{SHADOZ}$  reach approximately 1.0 K, continuing in this way until the  
 232 end of the  $\bar{T}_{SHADOZ}$  profile (around 30.0 km).  $\bar{T}_{MERRA-2}$  appears as a combination between  $\bar{T}_{SHADOZ}$  and  $\bar{T}_{COSMIC-1}$ , following

233 the behavior of SHADOZ in the first 30.0 km, so that the average profiles do not present a difference greater than 2.0 K, and  
 234 follows COSMIC-1 in the rest of the profile. Such behavior was also observed by Tegmeier et al. (2020). The similarity of  
 235  $T_{MERRA-2}$  with  $T_{SHADOZ}$  and  $T_{COSMIC-1}$  is justified by the composition of the MERRA-2 reanalysis data, since in addition to  
 236 being based on balloon-sonde profiles, these reanalysis data incorporate GPS-Radio Occultation information, which did not  
 237 happen with the original MERRA data.



238  
 239 **Figure 6:** (a) Global average temperature profiles over Réunion site from SHADOZ (red line), COSMIC-1 (green line) and MERRA-  
 240 2 (blue line), framed with their  $\pm 2\sigma$  (standard deviation) profiles (in coloured shadows). (b) Difference profiles:  
 241  $(\bar{T}_{SHADOZ} - \bar{T}_{MERRA-2})$  and  $(\bar{T}_{SHADOZ} - \bar{T}_{COSMIC-1})$ , respectively in black and orange lines.

242

#### 243 4. 4 Seasonal Comparison

244 As reported by several authors (Seidel et al., 2001; Bencherif et al., 2006; Sivakumar et al., 2011a; Bègue et al., 2010;  
 245 Shangguan and Wang, 2022; Zhran and Mousa., 2023), the thermal structure of the atmosphere is seasonally dependent,  
 246 notably in the tropics and subtropics. Thus, we examined and compared temperature profiles averaged by season (summer -  
 247 DJF, autumn -MAM, winter -JJA and spring -SON). Plots in the upper panel of Figure 7(a—d) superimpose the seasonal

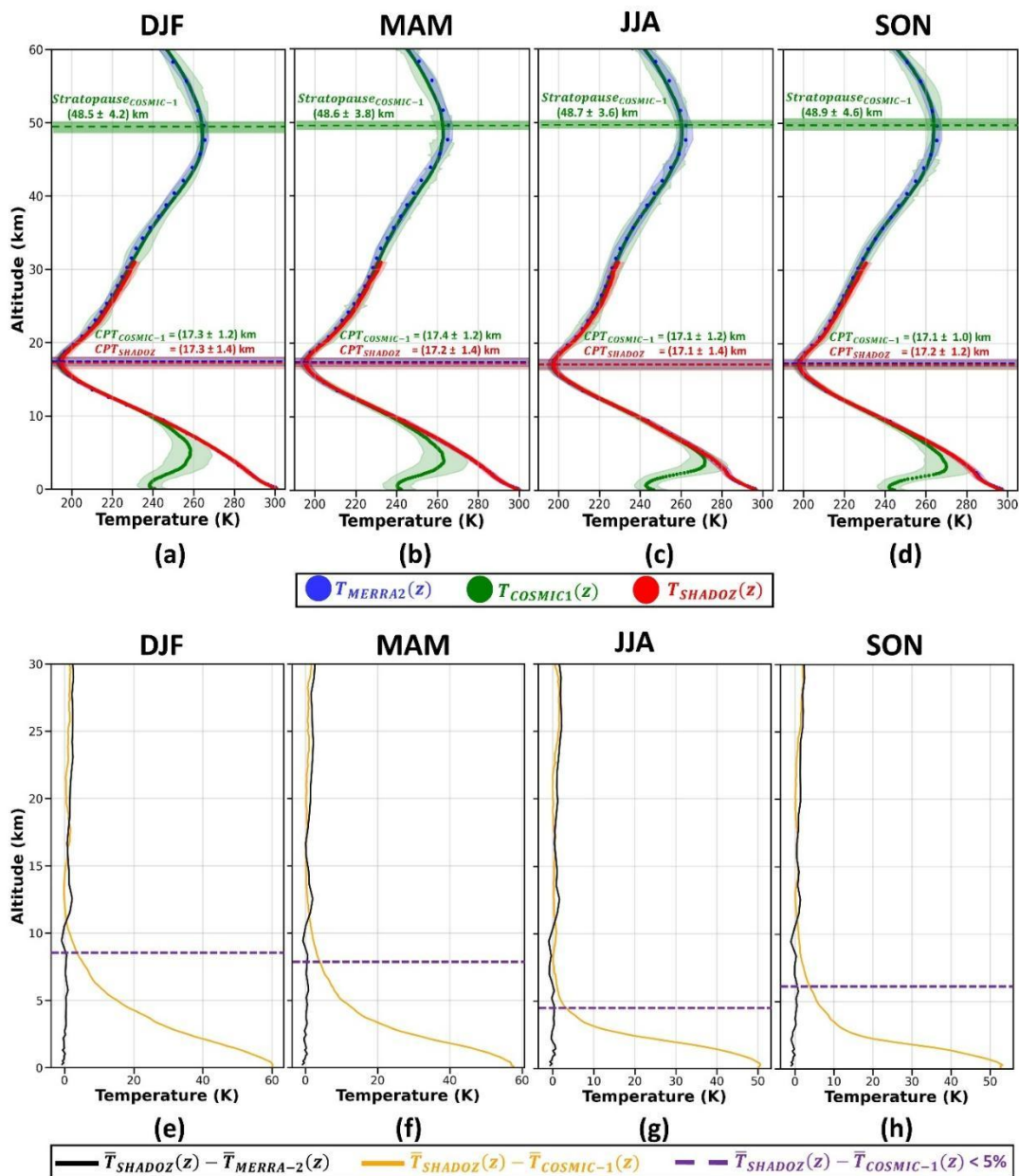
248 temperature profiles obtained from SHADOZ, COSMIC-1 and MERRA-2 and the associated seasonal temperature differences  
249 with the SHADOZ data as a reference (plots of the lower panel of Fig. 7e - h).

250 The altitude range of agreement between the seasonal  $\bar{T}_{SHADOZ}$  and  $\bar{T}_{COSMIC-1}$  temperature profiles vary depending on the  
251 season, as indicated in Figure 7(b). To enable comparison between different seasons, a horizontal dashed line is added to the  
252 temperature difference profiles. This line shows the altitude at which the temperature difference between  $\bar{T}_{SHADOZ}$  and  
253  $\bar{T}_{COSMIC-1}$  begins to be lower than 5%. It appears from this line that the altitude of validity of the COSMIC-1 measurements  
254 depends on the season. It is possible to identify a seasonal behavior, where the highest limit occurs in summer (5.3 km), then  
255 it decreases continuously, reaching 4.3 km in Autumn, and the lowest value in winter and spring (2.8 km). The best agreement  
256 between  $\bar{T}_{SHADOZ}$  and  $\bar{T}_{COSMIC-1}$  values are observed during the dry season (JJA), while during the wet season (DJF)  $\bar{T}_{COSMIC-1}$   
257 profiles seem to underestimate the  $\bar{T}_{SHADOZ}$  values over the widest range of altitudes. On the other hand, the difference between  
258  $\bar{T}_{SHADOZ}$  and  $\bar{T}_{MERRA-2}$  does not present a seasonality. During all seasons, the differences do not exceed 3.0 K. The higher  
259 values are observed between 11.0 and 14.0 km, and above 19.0 km. In these regions difference between  $\bar{T}_{SHADOZ}$  and  $\bar{T}_{MERRA-2}$   
260 is higher than that one observed between  $\bar{T}_{SHADOZ}$  and  $\bar{T}_{COSMIC-1}$ .

261 The CPT values estimated by both databases are quite similar, so that when considering the uncertainty values, it can be stated  
262 that the seasonal values obtained from COSMIC-1 and SHADOZ are practically coincident. The  $CPT_{COSMIC-1}$  sometimes  
263 overestimates and at others underestimates the  $CPT_{SHADOZ}$ . The lower absolute difference between them is observed during  
264 the Winter (26 m), and the higher one in Autumn (122 m). The average  $CPT_{SHADOZ}$  has a seasonal behavior similar to that one  
265 observed by Seidel et al. (2001), where the maximum and minimum values were observed in Summer and Winter, respectively.  
266 Bègue et al. (2010) also identified the maximum  $CPT_{SHADOZ}$  during the summer, as well as Astudillo et al. (2020) using  
267 Ground-Based GNSS Observations and Schmidt et al. (2004) using GPS RO data from the German CHAMP (CHALLENGING  
268 Minisatellite Payload) satellite mission. This seasonal tropopause behavior also was observed by Sivakumar et al. (2011a),  
269 which identified the minimum  $CPT_{SHADOZ}$  during the winter, and Zhran and Mousa (2023). On the other hand, although the  
270 lowest values of  $CPT_{COSMIC-1}$  occur during winter, in agreement with the results obtained by Seidel et al. (2001) and Sivakumar  
271 et al. (2011a), the maximum values occur in autumn, what is not in agreement with the current literature. It is important to  
272 highlight that this seasonal behaviour reinforces the influence of solar radiation in tropopause height, mainly in tropical and  
273 subtropical regions (Sivakumar et al., 2011a).

274 Regarding the  $CPT_{SHADOZ}$  temperature, the average monthly values obtained are similar, although a little bit smaller than those  
275 estimated by Bègue et al. (2010), so that the lower and higher mean absolute difference are -0.1 K (February, the coldest month  
276 identified by Bègue et al. (2010)) and -1.5 K (September, the hottest month identified by Bègue et al. (2010)), respectively. In  
277 this work the coldest month is January ( $[193.1 \pm 4.6]$  K) and the hottest is October ( $[197.1 \pm 4.6]$  K). Considering  $CPT_{COSMIC-1}$ ,  
278 excepting May, where the average  $CPT_{COSMIC-1}$  is 2.7 K higher than the  $CPT_{SHADOZ}$  obtained by Bègue et al. (2010), all other  
279 months have a smaller average temperature value, so that the lower and higher absolute difference are -0.3 (August) and -2.7

280 (April), respectively. The coldest and the hottest month are February ( $[192.1 \pm 4.6]$  K) and September ( $[197.5 \pm 4.8]$  K), as  
 281 observed by Bègue et al. (2010), respectively.



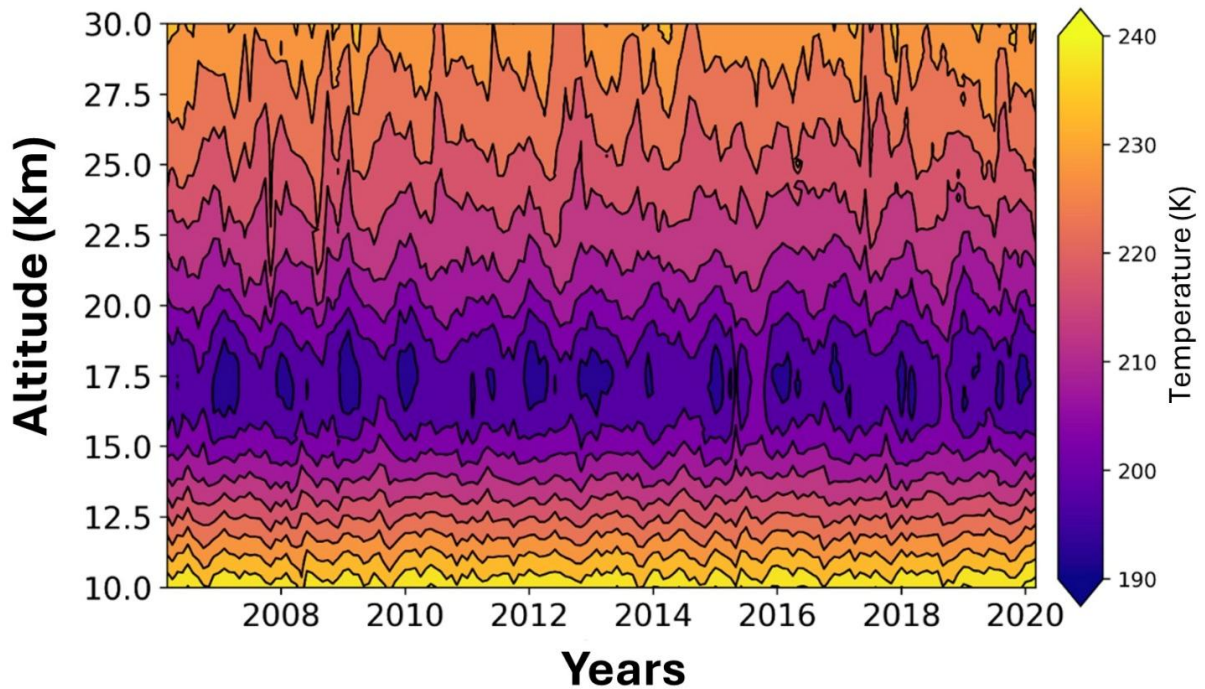
282  
 283 **Figure 7:** In the upper part is presented a seasonal comparison ((a) DJF, (b) MAM, (c) JJA, and (d) SON) among  $T_{SHADOZ}(z)$  (red),  
 284  $T_{COSMIC-1}(z)$  (green) and  $T_{MERRA-2}(z)$  (blue) profiles, and their respective standard-deviations. In the lower part is presented a  
 285 seasonal comparison ((e) DJF, (f) MAM, (g) JJA, and (h) SON) among the differences of  $T_{SHADOZ}(z)$  and  $T_{MERRA-2}(z)$  (black line)  
 286 and  $T_{SHADOZ}(z)$  and  $T_{COSMIC-1}(z)$  (orange line). The dotted purple line represents the height where the difference between  
 287  $T_{SHADOZ}(z)$  and  $T_{MERRA-2}(z)$  is lower than 5%.

288

289 Due to the necessity of data above 40 km, only  $T_{COSMIC-1}$  was applied to estimate the stratopause height, as indicated previously  
290 in section 3.3. The stratopause appears to be highest in spring ( $[48.9 \pm 4.6]$  km) with a maximum temperature of  $[266.3 \pm 0.4]$   
291 K, whereas it is lowest in summer ( $[48.5 \pm 4.2]$  km) with a temperature maximum of around  $[267.2 \pm 0.8]$  K. These results  
292 agree with the outcomes of other studies conducted at tropical locations. Batista et al. (2009) analyzed 14 years (from 1993 to  
293 2006) of temperature profiles recorded by a sodium resonance LiDAR at São José dos Campos, Brazil (23°S, 46°W). They  
294 found that the local stratopause altitude was  $\sim 49$ km, with the maximum temperature varying from 265 to 270K. Moreover,  
295 Sivakumar et al. (2011b) used temperature profiles over Réunion recorded between 1994 and 2007 by a Rayleigh LiDAR and  
296 reported that the stratopause height occurrence was in the 47–49 km height range, with temperatures ranging from 260 K to  
297 270 K. In addition, the same seasonal behaviour of the stratopause height presented in Figure 6 was observed by France et al.  
298 (2012) and Vignon et al. (2015) in their climatology studies using the Microwave Limb Sounder (MLS) and reanalysis data  
299 (MERRA-2).

#### 300 **4. 5 Combination between SHADOZ and COSMIC-1 datasets**

301 Considering the results presented in the previous section, where SHADOZ and COSMIC-1 temperature profiles showed a  
302 good agreement in the 10-28 km altitude range, we merged the two datasets to construct quasi-continuous and regular space-  
303 by-time matrix temperature values. SHADOZ and COSMIC-1 have different temporal resolutions (1 profile per week and 1  
304 profile every 2 days, respectively), as mentioned in Section 4.2. Therefore, the final database was created from the combination  
305 of these two datasets, and for days where there is data from both instruments, only the SHADOZ data were considered. Then,  
306 the daily temperature series obtained were reduced to monthly and kilometric averages and are presented in Figure 8. This new  
307 dataset will be applied in the trend analyses (section 5).



308

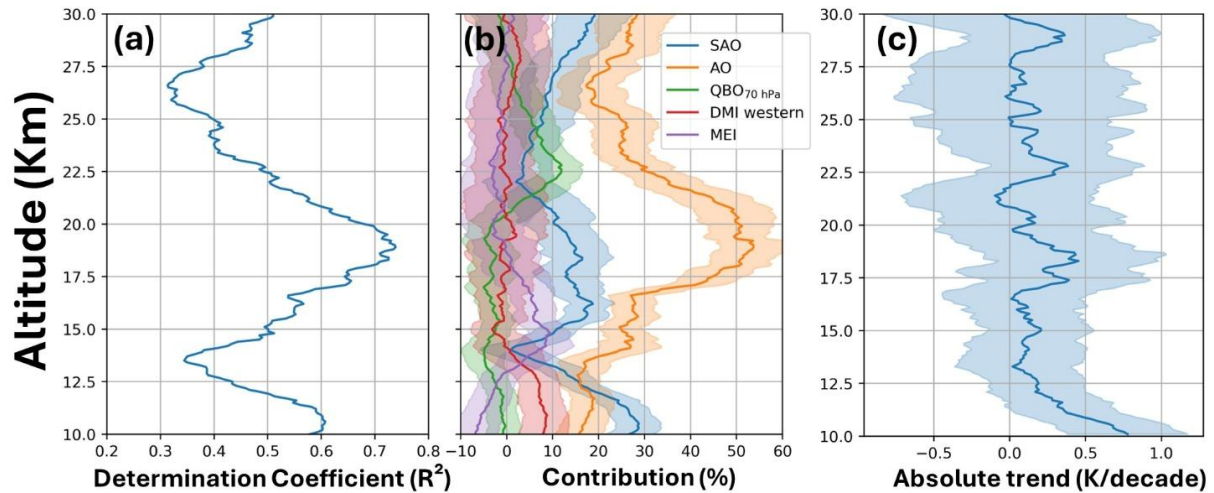
309 **Figure 8: Monthly time-height temperature cross-section over Réunion constructed by combining SHADOZ and COSMIC-1**  
 310 **profiles.**

### 311 **5 Trend Model Analysis**

312 For trend analysis, we used the multiple linear regression method taking into account the same *forcings* used by Bègue et al.  
 313 (2010) and by Tohir et al. (2018): annual and semi-annual cycles, quasi-biennial oscillation, and ENSO (section 3.4).

314 The analysis of the  $R^2$  profile, as depicted in Fig.8a, reveals two layers where the Trend-Run model performs well and explains  
 315 more than 65% of the temperature variability: one layer at around 10 km and another at around 18 km. Additionally, the  $R^2$   
 316 profile shows two minima ( $\sim 40\%$ ), where the Trend-Run model performs less well, in the upper troposphere (14 km) and the  
 317 upper stratosphere (26–27 km). This result is not surprising given the short length of the time series (2006–2020). We then  
 318 examine temperature trends in two tropospheric heights (10 km and 15 km) and two stratospheric layers (19 km and 24 km),  
 319 in addition to temperature trends at the local tropopause. Figure 8b overlays the profiles of the considered *forcings* as derived  
 320 from the Trend-Run model. Overall, the annual oscillation (AO) emerges as the most dominant forcing, particularly in the  
 321 lower stratosphere, where it accounts for over 40% of the variability at approximately 19 km. The semi-annual oscillation  
 322 (SAO) exhibits its maximum contribution in the troposphere, specifically at 10–11 km. The ENSO forcing displays an absolute  
 323 maximum contribution of -20 % in the lower stratosphere (22–23 km) and has a nearly constant contribution of approximately

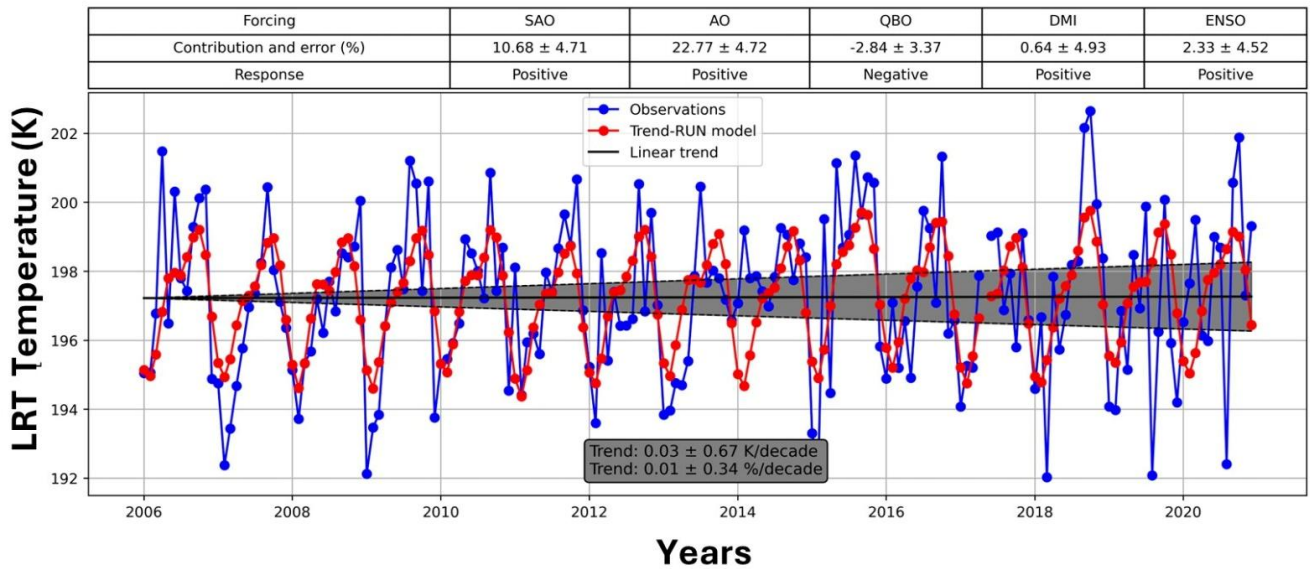
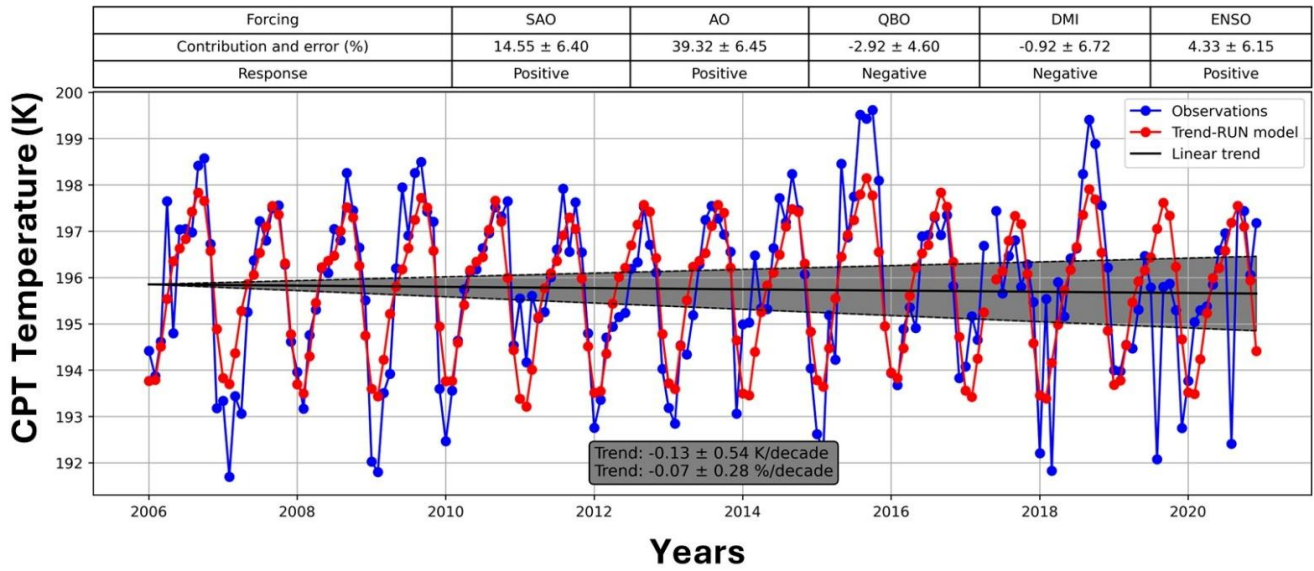
324 10% in the troposphere. The QBO index, obtained for the 70-hPa pressure level, shows almost no contribution in the  
 325 troposphere and a quasi-constant contribution in the stratosphere (~4%).  
 326 Following Figure 9(a), the higher determination coefficient can be observed in the UTLS region (18 – 20 km), so the higher  
 327 contribution, in this region, in the trend model is from AO (Fig. 9b). In addition, such a region presents an increase of around  
 328 0.25 K/decade (Fig. 8c).  
 329



330  
 331 **Figure 9: (a) autocorrelation coefficient profile, (b) vertical profile of contribution of each forcing, (c) vertical profile of absolute**  
 332 **variation of temperature per decade.**

333 Figure 10 shows temperature trends at the tropopause, CPT (Fig.10a) and LRT (Fig.10b) as well as, their standard deviations  
 334 at the  $2\sigma$  level (dotted line). So that the standard deviation associated with the trend value corresponds to uncertainty in the  
 335 trend slope. Temperature at the CPT presents a decreasing trend of  $[-0.13 \pm 0.27]$  K/decade, where seasonal cycles (AO, SAO)  
 336 seem to be the most dominant forcing Zou et al. (2023), using ERA5 data, observed a tropopause cooling of  $[-0.09 \pm 0.03]$   
 337 K/decade from 1980 to 2021. Although the time interval (1979-2005) is different from the present study, Tegtmeier et al.  
 338 (2020) reported a cooling of the tropical CPT from -0.3 to -0.6 K/decade.

339  
 340  
 341



342

343 **Figure 10: Trend model of CPT (a) and LRT (b) temperature variation. The black lines represent the trend of CPT and LRT**  
 344 **temperature, in figures a and b, respectively. The dotted black lines, in both figures, represent the standard deviation of the**  
 345 **temperature trend at the  $2\sigma$  level.**

346

347 On the other hand, LRT temperature (Fig. 10) shows a little insignificant increase ( $[0.03 \pm 0.33]$  K/decade), where in the same  
 348 way as CPT temperature, the seasonal cycles (AO, SAO) are the most dominant forcing. Shangguan and Wang (2022) and  
 349 Negash and Raju (2024) also observed a strong influence of AO and SAO in the UT-LS region from COSMIC-1 and ERA-5

350 data, and COSMIC-1 and Radiosonde data respectively in subtropical latitudes. Following Frierson (2006), the latent heat  
351 release caused by thermal forcing in the troposphere is what creates the strong AO in temperature. In addition, according to  
352 van Loon and Jene (1969), tropical and sub-tropical SAO are most pronounced in the areas where the Intertropical Convergence  
353 Zone crosses the Equator twice a year, in particular, from Eastern Africa to the central Pacific Ocean, which coincides with  
354 the region where Réunion is located.

355 Furthermore, it is important to highlight that the observed trends for both the CPT (cooling) and the LRT (warming)  
356 temperatures are directly associated with tropospheric warming, which has been exacerbated by intense accumulation of GHG  
357 in the lower troposphere as described by Ladstädter et al., 2023. This phenomenon is a key indicator of climate change and  
358 has been observed globally (Ladstädter et al., 2025), reinforcing the intense effect of anthropogenic activities across the planet.

## 359 **6 Conclusions**

360 Tropopause temperature and height serve as key indicators of anthropogenic climate change, influenced by factors such as  
361 stratospheric ozone, greenhouse gas concentrations, and volcanic activity. However, monitoring their variability remains  
362 challenging due to the sparse distribution of observation stations, particularly in the Southern Hemisphere. To address this, we  
363 compared temperature profiles from three datasets—SHADOZ, COSMIC-1, and MERRA-2—to assess their similarities and  
364 differences and to develop a refined dataset for trend analysis. Our analysis of SHADOZ and COSMIC-1 data (2006–2020)  
365 revealed strong agreement in temperature profiles above 10 km. MERRA-2 data showed a good correlation with SHADOZ up  
366 to 30 km and with COSMIC-1 above 30 km, but its coarse vertical resolution limited its applicability for tropopause height  
367 estimation. Using the Cold Point Tropopause (CPT) and Lapse Rate Tropopause (LRT) methods, we found that CPT-derived  
368 tropopause heights and temperatures were consistent across SHADOZ and COSMIC-1, whereas LRT values varied more due  
369 to differences in vertical resolution. Comparisons within each dataset confirmed that LRT-derived tropopause heights were  
370 systematically lower than those from CPT, while LRT temperatures were higher—consistent with previous studies.  
371 Additionally, CPT exhibited seasonal variability, with higher values in summer and lower values in winter. To enhance data  
372 coverage, we created a new dataset by integrating COSMIC-1 data into SHADOZ profiles between 10 and 30 km, preserving  
373 the seasonal characteristics observed in both datasets. This combined dataset improves the representation of tropopause  
374 dynamics in regions with sparse observations. Trend analysis highlighted the significant influence of the annual oscillation  
375 (AO), particularly in the upper troposphere–lower stratosphere (UT-LS) region. We observed a decreasing trend in CPT  
376 temperature ( $-0.13 \pm 0.27$  K/decade) and a slightly increasing trend in LRT temperature ( $0.03 \pm 0.33$  K/decade), both  
377 predominantly influenced by AO and the semi-annual oscillation (SAO). Our findings demonstrate the value of COSMIC-1  
378 data in studying tropopause dynamics, enabling the extension of time series in regions with radiosonde observations and  
379 providing critical data where in situ measurements are unavailable. This study underscores the potential of satellite-based  
380 remote sensing to enhance our understanding of climate-related changes in the tropopause.

381 **References**

- 382 Anthes, R. A., Bernhardt, P. A., Chen, Y., Cucurull, L., Dymond, K. F., Ector, D., Healy, S. B., Ho, S., Hunt, D. C., Kuo, Y.,  
383 Liu, H., Manning, K., McCormick, C., Meehan, T. K., Randel, W. J., Rocken, C., Schreiner, W. S., Sokolovskiy, S. V.,  
384 Syndergaard, S., Thompson, D. C., Trenberth, K. E., Wee, T., Yen, N. L., and Zeng, Z. The COSMIC/FORMOSAT-3 Mission:  
385 Early Results. *Bulletin of the American Meteorological Society*, 89(3), 313-334, 2008.
- 386 Astudillo, J. M., Lau, L., Tang, Y. T., and Moore, T. A novel approach for the determination of the height of the tropopause  
387 from ground-based GNSS observations. *Remote Sensing*, 12(2), 2020.
- 388 Austin, J., and Reichler, T. J. Long-term evolution of the cold point tropical tropopause: Simulation results and attribution  
389 analysis, *J. Geophys. Res.*, 113, D00B10, 2008.
- 390 Baldy, S., Ancellet, G., Bessafi, M., Badr, A. and Lan Sun Luk, D. Field observations of the vertical distribution of tropospheric  
391 ozone at the Island of La Réunion, *J. Geophys. Res.*, 101, 23835–23849, 1996.
- 392 Bègue, N., Bencherif, H., Sivakumar, V., Kirgis, G., Mze, N., and Leclair de Bellevue, J. Temperature variability and trends  
393 in the UT-LS over a subtropical site: Réunion (20.8° S, 55.5° E), *Atmos. Chem. Phys.*, 10, 8563–8574, 2010.
- 394 Bencherif, H., Diab, R., Portafaix, T., Morel, B., Keckhut, P., and Moorgawa, A. Temperature climatology and trend estimates  
395 in the UTLS region as observed over a southern subtropical site, Durban, South Africa, *Atmos. Chem. Phys.*, 6, 5121–5128,  
396 2006.
- 397 Birner, T., Sankey, D. and Shepherd, T. G. The tropopause inversion layer in models and analyses, *Geophys. Res. Lett.*, 33,  
398 L14804, 2006.
- 399 Britannica, 2025. Available at <https://www.britannica.com/place/Réunion>. Accessed on 8 may. 2025.
- 400 Dickey, D. A. and Fuller, W. A. Distribution of the Estimators for Autoregressive Time Series with a Unit Root. *Journal of*  
401 *the American Statistical Association*, 74 (366), 427–431, 1979.
- 402 France, J. A., Harvey, V. L., Randall, C. E., Hitchman, M. H., and Schwartz, M. J. A climatology of stratopause temperature  
403 and height in the polar vortex and anticyclones, *J. Geophys. Res.*, 117, D06116, 2012.
- 404 Frierson, D.M. Robust increases in midlatitude static stability in simulations of global warming. *Geophys. Res. Lett.*, 33 (24),  
405 2006.
- 406 Fueglistaler, S., Dessler, A. E., Dunkerton, T. J., Folkins, I., Fu, Q. and Mote, P. W. Tropical tropopause layer, *Rev. Geophys.*,  
407 47, RG1004, 2009.
- 408 Hoinka, K. P. Statistics of the Global Tropopause Pressure. *Mon. Wea. Rev.*, 126, 3303–3325, 1998.

409 Ladstädter, F., Steiner, A. K., and Gleisner, H. Resolving the 21st century temperature trends of the upper troposphere–lower  
410 stratosphere with satellite observations. *Sci. Rep.* 13, 1306, 2023.

411 Ladstädter, F., Stocker, M., Scher, S., and Steiner, A. K.: Observed changes in the temperature and height of the globally  
412 resolved lapse rate tropopause, *Atmos. Chem. Phys.*, 25, 16053–16062, <https://doi.org/10.5194/acp-25-16053-2025>, 2025.

413 Morioka, Y., Tozuka, T. & Yamagata, T. Climate variability in the southern Indian Ocean as revealed by self-organizing maps.  
414 *Clim Dyn* 35, 1059–1072, 2010.

415 Negash, T. and Raju, U.P. Study on long term troposphere lower stratosphere temperature (TLST) trend in tropical and  
416 subtropical northern hemisphere using ground based and COSMIC satellite data, *Journal of Atmospheric and Solar-Terrestrial*  
417 *Physics*, 261, 106306, 2024.

418 Randel, W. J., and Cobb, J. B. Coherent variations of monthly mean total ozone and lower stratospheric temperature, *J.*  
419 *Geophys. Res.*, 99(D3), 5433–5447, 1994.

420 Randel, W. J., F. Wu, and W. Rivera Ríos, Thermal variability of the tropical tropopause region derived from GPS/MET  
421 observations, *J. Geophys. Res.*, 108(D1), 4024, doi:[10.1029/2002JD002595](https://doi.org/10.1029/2002JD002595), 2003.

422 Randel, W., Jensen, E. Physical processes in the tropical tropopause layer and their roles in a changing climate. *Nature*  
423 *Geosci* 6, 169–176, 2013.

424 Reid, G. C., and K. S. Gage, On the annual variation in height of the tropical tropopause, *J. Atmos. Sci.*, 38, 1928±1938, 1981.

425 Reid, G. C., and K. S. Gage, A relationship between the height of the tropical tropopause and the global angular momentum  
426 of the atmosphere, *Geophys. Res. Lett.*, 1, 840-842, 1984.

427 Reid, G. C., and K. S. Gage, Interannual variations in the height of the tropical tropopause, *J. Geophys. Res.*, 90, 5629±5635,  
428 1985.

429 Saji, N., Goswami, B., Vinayachandran, P. et al. A dipole mode in the tropical Indian Ocean. *Nature* 401, 360–363, 1999.

430 Santer, B. D., et al. (2004), Identification of anthropogenic climate change using a second-generation reanalysis, *J. Geophys.*  
431 *Res.*, 109, D21104, 2004.

432 Schmidt, T., Wickert, J., Beyerle, G., and Reigber, C. Tropical tropopause parameters derived from GPS radio occultation  
433 measurements with CHAMP, *J. Geophys. Res.*, 109, D13105, 2004.

434 Selkirk, H. B, The tropopause cold trap in the Australian monsoon during STEP/AMEX 1987, *J. Geophys. Res.*, 98(D5), 8591–  
435 8610, 1993.

436 Seidel, D. J., Ross, R. J., and Angell, J. K. Climatological characteristics of the tropical tropopause as revealed by radiosonde,  
437 *J. Geophys. Res.*, 106, 7857–7878, 2001.

438 Shangguan, M. and Wang, W. The semi-annual oscillation (SAO) in the upper troposphere and lower stratosphere (UTLS),  
439 Atmos. Chem. Phys., 22, 9499–9511, 2022.

440 Sivakumar, V., Baray, J.-L., Baldy, S. and Bencherif, H. Tropopause characteristics over a southern subtropical site, Reunion  
441 Island (21°S, 55°E): Using radiosonde–ozonesonde data. J. Geophys. Res., 111, D19111, 2006.

442 Sivakumar, V., Bencherif, H., Bègue, N., and Thompson, A. M. Tropopause Characteristics and Variability from 11 yr of  
443 SHADOZ Observations in the Southern Tropics and Subtropics. J. Appl. Meteor. Climatol., 50, 1403–1416, 2011.

444 Sivakumar, V., Vishnu Prasanth, P., Kishore, P., Bencherif, H., and Keckhut, P. Rayleigh LIDAR and satellite (HALOE,  
445 SABER, CHAMP and COSMIC) measurements of stratosphere-mesosphere temperature over a southern sub-tropical site,  
446 Reunion (20.8° S; 55.5° E): climatology and comparison study, Ann. Geophys., 29, 649–662, 2011.

447 Sivakumar, V., Jimmy, R., Bencherif, H., Bègue, N., Portafaix, T. Use of the TREND RUN model to deduce trends in South  
448 African Weather Service (SAWS) atmospheric data: Case study over Addo (33.568°S, 25.692°E) Eastern Cape, South Africa.  
449 Journal of Neutral Atmosphere, 51- 58, hal-02098051, 2017.

450 Tegtmeier, S., Anstey, J., Davis, S., Dragani, R., Harada, Y., Ivanciu, I., Pilch Kedzierski, R., Krüger, K., Legras, B., Long,  
451 C., Wang, J. S., Wargan, K., and Wright, J. S.: Temperature and tropopause characteristics from reanalyses data in the tropical  
452 tropopause layer, Atmos. Chem. Phys., 20, 753–770, <https://doi.org/10.5194/acp-20-753-2020>, 2020.

453 Thompson, A. M., Witte, J. C., Sterling, C., Jordan, A., Johnson, B. J., Oltmans, S. J., and Thiongo, K. First reprocessing of  
454 Southern Hemisphere Additional Ozonesondes (SHADOZ) ozone profiles (1998-2016): 2. Comparisons with satellites and  
455 ground-based instruments. Journal of Geophysical Research: Atmospheres, 122, 13,000-13,025, 2017.

456 Tohir, A. M., Portafaix, T., Sivakumar, V., Bencherif, H., Pazmiño, A., and Bègue, N. Variability and trend in ozone over the  
457 southern tropics and subtropics, Ann. Geophys., 36, 381–404, 2018.

458 Vignon, E. and Mitchell, D. M. The stratopause evolution during different types of sudden stratospheric warming event. Clim.  
459 Dyn., 44, 3323–3337, 2015.

460 Witte, J. C., Thompson, A. M., Smit, H. G. J., Fujiwara, M., Posny, F., Coetzee, G. J. R., Northam, E. T., Johnson, B. J.,  
461 Sterling, C. W., Mohamad, M., Ogino, Shin-Ya, Jordan, A., and da Silva, F. First reprocessing of Southern Hemisphere  
462 ADditional OZonesondes (SHADOZ) profile records (1998-2015): 1. Methodology and evaluation, J. Geophys. Res. Atmos.,  
463 122, 6611-6636, 2017.

464 WMO (1957), Definition of the tropopause, WMO Bull., 6, 136.

465 Xia, P., Shan, Y., Ye, S., and Jiang, W. Identification of Tropopause Height with Atmospheric Refractivity. J. Atmos. Sci., 78,  
466 3–16, 2021.

- 467 Xian, T. and Homeyer, C. R. Global tropopause altitudes in radiosondes and reanalyses, *Atmos. Chem. Phys.*, 19, 5661–5678,  
468 2019.
- 469 Zhran, M. and Mousa, A. Global tropopause height determination using GNSS radio occultation, *The Egyptian Journal of*  
470 *Remote Sensing and Space Science*, 26, 2, 317-331, 2023.
- 471 Zhran, M., Mousa, A., Alshehri, F., and Jin, S. Evaluation of Tropopause Height from Sentinel-6 GNSS Radio Occultation  
472 Using Different Methods. *Remote Sens.*, 15, 5513, 2023.
- 473 Zou, L., Hoffmann, L., Müller, R., and Spang, R. Variability and trends of the tropical tropopause derived from a 1980–2021  
474 multi-reanalysis assessment. *Front. Earth Sci.*, 11:1177502, 2023.